From Grain Boundaries to Single Defects: A Review of Coherent Methods for Materials Imaging in the X-ray Sciences

BRIAN ABBEY[1,2,3]

1.—Department of Physics, La Trobe University, Melbourne, VIC 3086, Australia. 2.—Melbourne Centre for Nanofabrication, Melbourne, VIC 3168, Australia. 3.—e-mail: b.abbey@latrobe.edu.au

This review summarizes the literature describing recent advances in the coherent x-ray sciences for the high-resolution characterization of materials. The principles and some of the main experimental techniques as well as their applications are discussed. The advantages of x-ray methods for characterizing 3D microstructures as well as for characterizing plasticity in the bulk become clear from the examples presented. Materials that exhibit size effects within the 0.1–10-μm range benefit enormously from these techniques, and development of the relevant x-ray methods will add to our fundamental understanding of these phenomena. Many of the ideas that have developed in the coherent x-ray science literature have been enabled through advances in x-ray source and detection technology, which has occurred over the past 10 years or so. It is a topic of considerable importance to consider how these techniques, which have matured rapidly, may be best applied to materials imaging in order to meet the growing needs of the community. As coherent x-ray methods for characterizing materials at multiple length scales have developed, several key applications for these techniques have emerged. The key breakthroughs that have been enabled by these new methods are discussed throughout this review, together with an examination of some of the problems that will be addressed by these techniques within the next few years.

INTRODUCTION

X-rays have a clear advantage in materials science as a result of their ability to nondestructively probe the internal structure of optically opaque samples, provided of course that the sample is sufficiently radiation hard. X-rays have a long and rich history of development for materials applications. Perhaps one of the best known examples is elastic strain mapping, where an x-ray diffraction pattern is collected, and the measured peak positions are used to determine the change in the bulk lattice parameter compared with an unstrained reference.[1] X-ray microtomography is another common example where, provided there is sufficient contrast between features, a material's microstructure can be reconstructed in 3D.[2] It has also been demonstrated that strain mapping may be combined with tomography to obtain 3D images of the strain fields within bulk materials.[3] Until significant improvements in the resolution of x-ray techniques were realized, however, scientists often had to interpret data that represented an average of a large number of different material states within the measurement volume. Hence, for example, characterizing the subgrain deformation structure and single defects was beyond the reach of most x-ray imaging techniques. That has changed over the past decade with the advent of high-resolution x-ray detectors, hard x-ray micro or nano focusing, and the development of coherent diffractive imaging (CDI) techniques that allow nanometer-scale imaging of thick specimens.[4]

A particular area where the dramatic improvement in the spatial resolution of coherent x-ray techniques is having a large impact is in the investigation of so-called "size effects."[5] In materials science, size effects are taken to mean the modification of a sample's material properties as a direct consequence of its microstructure or overall dimensions. Size effects are often responsible for the

inaccuracy of many predictive models for material behavior and have been the subject of years of extensive investigation in the literature. A 1994 paper by Fleck in which a deformation theory for size effects is developed states that "In conventional plasticity theory no length scale enters the constitutive law and no size effects are predicted. However, several observed plasticity phenomena display a size effect whereby the smaller is the size the stronger is the response.… The effect becomes pronounced when the indent size, grain size or particle spacing lies below approximately 10 μm."[6] This statement encapsulates one of the biggest drivers for the development of the high-resolution x-ray techniques that are discussed in this review, and some of the examples provided actually highlight the significant differences that have been observed in material behavior between, for example, thin films and bulk materials.[7–9]

For many years, fundamental insights into materials behavior were largely driven by advances in electron microscopy (EM). The ability to study defects at near-atomic resolution or, with the later development of *in situ* TEM, characterize defect dynamics in real time has revolutionized our understanding of crystal plasticity.[10] However, the requirement for electron transparent samples does not allow for the study of bulk samples or samples that are any thicker than $\sim$1 μm. The majority of the length scales for which size effects are known to occur are thus inaccessible to electron methods without sectioning, which may mean the sample is no longer representative of the bulk material. This means that for many materials we currently lack the relevant information needed to accurately predict their deformation behavior. The alternative is to use x-rays; however, historically x-rays have lacked the necessary resolution or contrast mechanisms to deliver anything like the level of detailed information that EM can provide. With the current widespread availability of extremely bright sources of coherent x-rays, though, as well as the development of new methods for collecting and interpreting data, the materials science landscape is rapidly changing.

Today, x-ray techniques are used routinely to probe materials with feature sizes of 0.1–10 μm, in many cases at spatial resolutions approaching 10 nm. For example, phase contrast methods[11] can provide 3D images of the grain boundary structure; microbeam techniques allow dislocation networks and subgrain structures to be mapped in the bulk[12]; and CDI is enabling the characterization of the deformation due to individual crystallographic defects.[13] These developments by the x-ray community are providing a rich new source of information for materials science that will continue to grow into mainstream techniques. This review is intended both as a short introduction for the general reader to these techniques and as a guide to possible future research directions in the field.

Coherence

All x-ray sources have some degree of partial coherence; since this review is concerned with experimental methods in which these coherence effects are important, a brief introduction to the concept of coherence is now given. For a more in-depth discussion of these issues particularly in the context of imaging, the interested reader is directed toward a recent review by Nugent.[14] Coherence describes the degree of spatial and temporal correlation between two points on a wavefield. The degree of coherence can be determined from the interference visibility that results from superposition of the waves associated with these two points. The techniques discussed in this review essentially rely on the interference of scattered x-rays; if the wavefield is incoherent, these interference effects will be completely suppressed and these techniques will not work. For an x-ray undulator source, the degree of correlation between points in space (spatial coherence) is principally determined by the source size while the degree of correlation between points on the wavefield as a function of time (temporal coherence) is determined by the source divergence.

Textbook discussions of the subject of coherence frequently illustrate the concepts of coherence through Young's two slit experiment where the contrast of the fringes gives the degree of coherence. Figure 1 illustrates the Young's two slit experiment for the case of a wavefield with partial spatial coherence and a wavefield with partial temporal coherence. It can be seen that the effect of partial spatial coherence is to reduce the fringe visibility across the entire diffraction pattern while the effect of partial temporal coherence is to reduce the fringe visibility as a function of the diffraction angle. Often the effectiveness of the techniques described in this review relies on reducing these effects of partial coherence to the point where they are undetectable in the experiment.

PHASE CONTRAST TOMOGRAPHY (PCT)

Basic Principle and Method

Most metals in common usage are polycrystalline; the atoms within polycrystals are aligned into ordered regions known as grains, each with a specific crystallographic orientation. The grain orientations and the sharp flat walls that separate them (the grain boundaries) can have a profound influence on the deformation behavior of metals. For example, cracks tend to initiate and follow grain boundaries, while texturing can greatly influence the strength of polycrystals depending on load direction, grain size distribution, and shape.

Since many polycrystalline samples have fairly homogenous absorption characteristics, aside from diffraction, there are no obvious means for determining the grain structure from absorption alone or for monitoring the formation and propagation of

(a) Partial spatial coherence
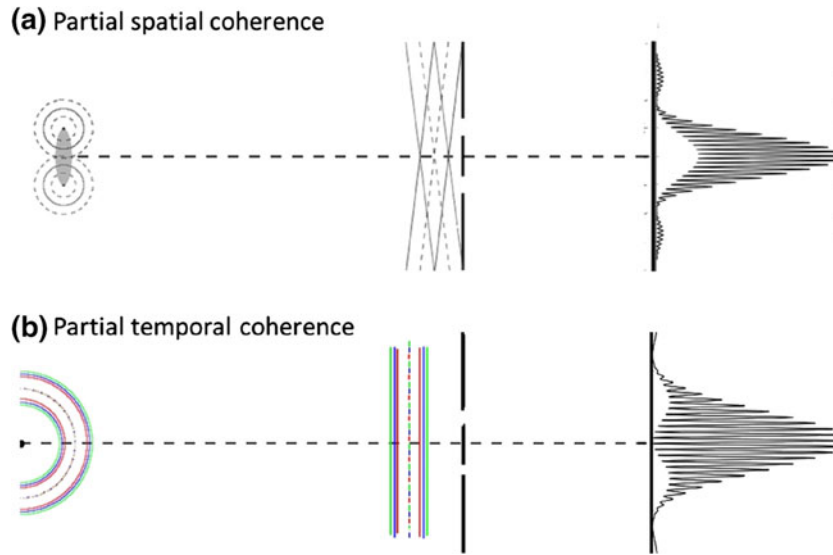
(b) Partial temporal coherence

Fig. 1. (a) Schematic illustrating the effect in a Young's two slit diffraction experiment of having a source with partial spatial coherence. Since the individual point sources that make up the extended source are uncorrelated, independent emitters, the interference visibility in the pattern is reduced everywhere. (b) Schematic illustrating the effect of partial temporal coherence. The fringe spacing for each wavelength comprising the source will be expanded or contracted depending on the diffraction angle leading to fringes with decreasing visibility at higher angles.

cracks. PCT exploits the modification to both the phase and the amplitude component of the incident x-rays propagating through the sample.[15] PCT generally relies on propagation-based enhancement of the phase component of the exit surface wave (ESW) transmitted at the exit face of the sample in comparison with the absorption component. The complex transmission function for the object is normally written as:

$$T(\vec{r}) = |T(\vec{r})| \exp(i\delta(\vec{r})kt(\vec{r}))$$
$$= \exp(-\beta(\vec{r})kt(\vec{r})) \exp(i\delta(\vec{r})kt(\vec{r})) \quad (1)$$

where $\beta(\vec{r})$ describes the absorption and $\delta(\vec{r})$ characterizes the phase change imparted to the ESW by interaction with the object. k and $t(\vec{r})$ are the associated wavenumber for the incident wavelength and object thickness, respectively. A useful expression for the intensity $I(\vec{r})$ of the sample ESW that captures many of the essential characteristics of propagation-based PCT is that derived by Pogany et al.[16] assuming perfect coherence at the sample:

$$I(\vec{r}) = [1 - 2\beta(\vec{r})] - \frac{Z}{k}\nabla^2\delta(\vec{r}) \quad (2)$$

In Eq. 2 we see that the modification of the propagated ESW intensity due to the phase is directly proportional to the propagation distance Z. We also note that the phase contrast is proportional to the Laplacian of $\delta(\vec{r})$, hence, at the edges or boundaries within the sample where there will be a rapid variation in the phase component of $T(\vec{r})$, and so contrast will be enhanced compared with homogeneous regions where $T(\vec{r})$ is slowly varying. This behavior has been confirmed by experiments performed at the European Radiation Synchrotron Radiation Facility (ESRF).[11,15]

When Z = 0, which is the "contact regime," the second term in Eq. 2 disappears and the phase-enhanced sensitivity to edge features disappears entirely, such that the image displays absorption contrast only. These characteristics of propagation-based phase contrast explain why grain boundaries and microcracks may be visible at sufficiently large propagation distances but not when the detector is within the contact regime of the sample. The abrupt change in the phase gradient between areas of high and low $\delta(\vec{r})$ produces interference fringes at the boundary between these two regions. Increasing the propagation distance by moving the detector further away from the sample means that the fringes become broader and more pronounced (this effect is illustrated in Fig. 2 and Table I, 1st row). Hence, unless propagation-based phase retrieval techniques such as "transport-of-intensity"[14] are applied to recover the ESW in the sample plane, this increase in contrast comes at the cost of spatial resolution. Phase contrast can yield dramatic improvements in the sensitivity of x-ray imaging to voids, cracks, and cavities. For example, the smallest detectable void (giving 1% contrast) in bulk aluminium at 25 keV is around 20 μm using absorption contrast. Using phase contrast, however, the smallest detectable void in aluminum is reduced to just 0.05 μm.[17]

To observe a measurable phase contrast component in the ESW, the incident illumination must be partially coherent. Based on the earlier work of Pogany et al. and Guigay,[16,18,19] Nugent[14] provides an estimate of the spatial coherence length required to maximize the phase contrast for a given spatial resolution defined by the maximum spatial frequency, q_{max}, present in the sample image. Without any optical magnification of the ESW, the value for q_{max}
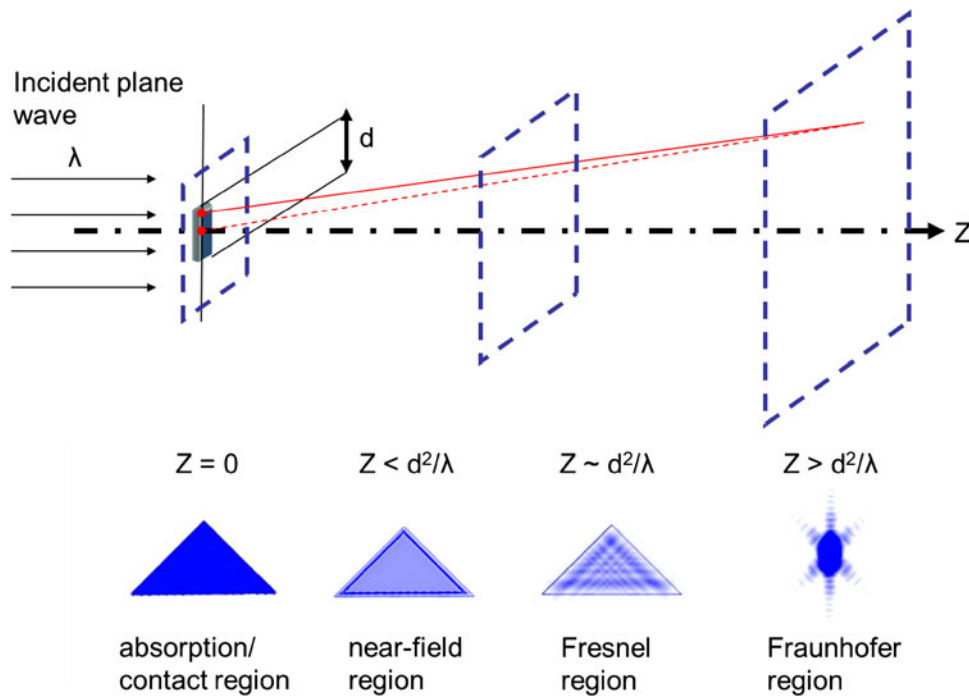
Fig. 2. Illustration of the absorption, near-field, Fresnel and Fraunhofer regions that occur for a plane-wave incident upon a sample depending on the propagation distance between the sample and the detection planes.

depends on the inverse of $2\Delta_d$, where Δ_d is the detector pixel width. Assuming a relatively small propagation distance such that $\left(2\pi^2|q_{max}|^2Z\right)/k \ll 1$, the spatial coherence length, l_c^{sp}, must satisfy:

$$l_c^{sp} \geq \frac{Z}{\lambda}q_{max} \tag{3}$$

So for smaller values of λ (wavelength) or higher resolution images, the coherence requirements to observe phase contrast become increasingly stringent. Similarly as Z increases and the phase contribution in Eq. 2 increases, longer coherence lengths are required. Hence, at very short sample-to-detector distances, the coherence requirements for PCT are relatively easy to satisfy at third-generation synchrotrons since the optical path length differences at small Z are also very small.[20]

Another important emerging technique for visualizing the grain structure that is worth mentioning here is that of diffraction contrast tomography (DCT) in which individual grains and their orientations are determined from their x-ray diffraction characreristics.[21] In DCT, the sample is rotated about a single-axis n over $360°$ while illuminated by a planar monochromatic beam that results in each grain within the sample satisfying the diffraction condition multiple times. Each grain produces Friedel pairs of diffraction spots (hkl and $\overline{hkl}$) observed at rotation angles of ω and $\omega + 180°$.[22,23] Using this approach, 3D grain mapping and indexation in polycrystalline samples containing up to a few thousand grains is possible. Due to the relatively modest coherence requirements, in comparison with the majority of methods described here, this technique is not covered any further within this review. However, the interested reader is directed toward a summary of the DCT method by Ludwig et al.[21]

Applications to Materials Imaging

In 1997, Cloetens et al.[24] demonstrated the 3D visualization of microcracks in a metal–matrix composite fiber using the ID19 beamline at the ESRF. The crack formation, growth, and eventual failure of the SiC fiber were measured at a single deformation state equivalent to 1% plastic strain (Fig. 3). PCT was used to create tomographic images of the structure of paper in 2002 at ID22 (ESRF) and to perform laminography of an integrated circuit in the same year.[25] In 1997, 1999, and 2006, Buffiere et al. and Baruchel et al. performed interrupted fatigued tests to monitor the 3D *in situ* growth of fatigue cracks induced in aluminum alloys (Fig. 4), interpreting the results using finite element methods.[26–28] In 2005, the microstructural evolution of ceramic samples were studied during sintering performed at temperatures in excess of $700°$ using phase contrast microtomography.[29] From this data, quantitative information such as the degree of porosity was determined. Phase contrast imaging has also found applications in the study of high-speed liquid jets and sprays using a combination of high-spatial and time resolution detection.[30] Such work represents the very latest in development of time-resolved synchrotron technology and imaging.

Table I. Brief summary of main techniques discussed in this review

Method	Schematic of Setup	Comments	Selected References*
Phase contrast Tomography		Can image 3D cracks and grain boundaries in mm-sized samples. Resolution ∼l μm, detector limited. Normally, propagation based phase contrast, can be quantitative.	Pogany et al.[16] Cloetens et al.[24] Buffiere et al.[27] Baruchel et al.[26]
Plane-wave coherent diffractive imaging		Can image small isolated objects. Loss of low-q information. 10-nm resolution with 0.1 nm possible at XFELs, limited by NA of reconstructed ESW.	Sayre[32] Fineup[33] Miao et al.[31,42] Chapman et al.[36] Turner et al.[47]
Ptychographic coherent diffractive imaging		Can image extended objects. Requires multiple diffraction patterns, so no single shot. Quantitative, recover illumination. Down to 10-nm resolution.	Faulkner et al.[52] Rodenburg et al.[57] Thibault et al.[58,92] Schropp et al.[56]
Diverging beam coherent diffractive imaging		Can image extended objects. Single-shot experiments. 10-nm resolution with 1 nm possible at XFELs. Quantitative, recover illumination.	Nugent et al.[63] Quiney et al.[67] Williams et al.[63,72] Abbey et al.[73,75] Putkunz et al.[77]
Microbeam x-ray coherent diffraction		Can image extended objects. Modest coherence requirements. Resolution optics limited >0.1 μm. Can study highly deformed samples.	Ravy et al.[102] Abbey et al.[7] Hofmann et al.[101] Jacques et al.[104]
Bragg coherent diffractive imaging		Can image small, isolated, single-crystal samples. 10-nm resolution with 0.1 nm possible at XFELs. Weakly strained objects only.	Robinson et al.[106] Pfeifer et al.[107] Harder et al.[13] Godard et al.[108] Newton et al.[110]

* Note that the selected references are meant to give the general reader a historical and applied overview. Many important works have thus necessarily been omitted for the sake of brevity. Partially CDI is omitted as it is equally applicable to most of these experimental geometries.

PLANE-WAVE CDI

Basic Principle and Method

X-rays generally only have weak interactions with matter. This makes them both extremely useful for imaging bulk materials but also difficult to manipulate and to focus. In addition, x-ray absorption contrast, particularly for biological samples, can be low in comparison with, for example, EM. Hence, there is a strong motivation for developing phase-sensitive x-ray imaging techniques that can provide high-spatial resolutions, similar to x-ray
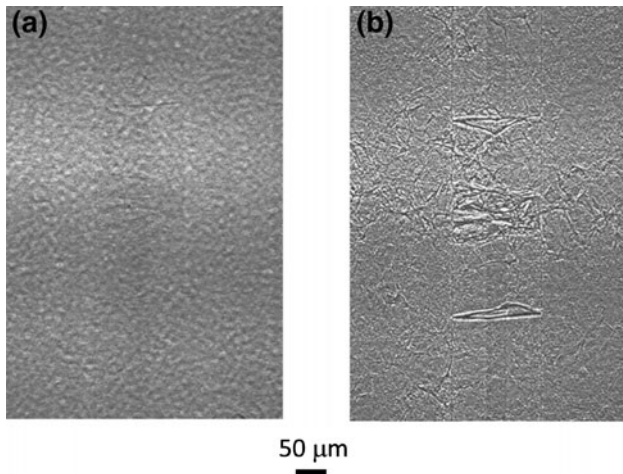
Fig. 3. Demonstration of propagation enhanced phase contrast in a monofilament Al/SiC composite. The x-ray energy was 25 keV, and the propagation distance was (a) 0.005 m and (b) 0.13 m. This shows just one projection from a PCT series used to reconstruct cracks in the fiber structure in 3D at a fixed 1% plastic strain. (Reprinted with permission from Ref. 24, Copyright © 1997 by the American Institute of Physics.)
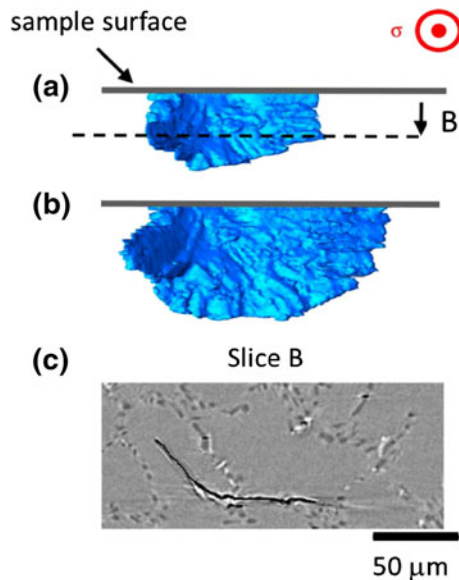

Fig. 4. Images of a fatigue crack growing from the surface inside a cast Al alloy: (a) 3D rendering of the crack surface as seen along the stress direction after 270,000 and after (b) 285,000 fatigue cycles; (c) reconstructed 2D slice (along B, as indicated in (a)) showing a strong deviation of the crack front induced by a grain boundary. (Reprinted with permission from Ref. 26, Copyright © 2006 by Elsevier.)

crystallography, but without the need for highly ordered crystals. The rapid development of coherent x-ray imaging methods that use the continuous diffraction from arbitrary samples, whether periodic or not, has now come a long way in addressing these aims.

While x-ray crystallography has long been established as a means for recovering the molecular structure from crystals, it was as recent as 1999 that Miao et al.[31] demonstrated experimentally that the crystallographic method could be extended to include samples with no inherent periodicity. This technique is commonly referred to as CDI. Since the first early experiments, there has been an outpouring of activity within the x-ray imaging community as the opportunities, challenges, and variations on the original concept have been explored. The key to this technique is in the "oversampling" of the measured diffraction signal that, from a crystallographer's point of view, may be regarded as measuring the intensity between diffraction spots as well as at the spots themselves. The idea stems from a 1952 paper by Sayre[32] in which he realized that Shannon's sampling theorem implies that an object can be reconstructed provided its diffraction signal is sufficiently "oversampled." It is natural to wonder why almost 50 years passed since the publishing of Sayre's paper and the first experimental realization of this idea. Part of the reason was technological, the fidelity of transferring information from x-ray-sensitive plates or film is not sufficient for CDI; hence, modern detectors such as a charge coupled device are required for detection. Second, the implementation of CDI reconstruction algorithms involves repeated executions of the fast Fourier transform; without the advent of modern personal computers, this proved a significant barrier for many researchers.

The topic of algorithms for phasing continuous diffraction patterns in order to recover the ESW for isolated objects has been covered in a number of reviews, including a very well-known 1987 paper by Fienup.[33] In most cases, with the notable exception of ptychography (see the subsequent discussion), recovering the sample ESW consists of the repeated application of two constraints. Namely, the imposition of the measured Fourier modulus in the detector plane ESW (the "modulus constraint") and the restriction of the extent of the sample to some finite region representing the total area of the diffracting object known as the "support" (the "support constraint"). The error reduction (ER) algorithm, which closely resembles the Gerchberg–Saxton approach[34] in which the object's intensity distribution is assumed as *a priori* information, is the earliest and best known of the algorithms used in CDI. The first ER algorithms used to reconstruct an image in CDI, however, were extremely slow to converge to a solution, and so a lot of work within the field has gone into developing robust methods for phasing the diffraction data. The hybrid input–output algorithm in which a feedback parameter from the previous sample ESW estimate is included at each iteration has been particularly successful.[33] Other common variations include the difference map algorithm by Elser[35] or relaxed averaged alternating reflectors algorithm by Chapman.[36] For further details on CDI algorithms, the reader is directed to a comprehensive review of the topic by Marchesini.[37]

The success of CDI as a high-resolution microscopy tool has produced a large number of different experimental varieties and implementations. Only the main cases will be covered in this review, and to begin with, it is appropriate to describe the simplest, from an experimental point of view, version of the technique. That is the illumination of a small, usually micron-sized sample, by a quasi-monochromatic and spatially coherent plane wave. The detector is placed in the far field of the isolated object to be imaged and at a sufficient distance that its diffraction pattern is oversampled (a schematic can be found in Table I, 2nd row) at twice the Nyquist frequency—the highest spatial frequency recorded on the detector, q_{max}. As a guide to performing an actual experiment, it is useful at this point to relate the oversampling requirement to some common experimental parameters. If the maximum dimension d of the sample we wish to image is too large, the highest spatial frequencies in the autocorrelation will become wrapped and appear to overlap the lowest spatial frequencies. This corresponds to an undersampling of the sample's diffracted intensities. Therefore, the sampling theory imposes the constraint that $d < N\Delta_s/2$, where N is the total number of sampling points across the array containing the object and Δ_s is the distance between neighboring points. If this condition is met, the Fourier transform of the diffraction intensities will yield an unaliased autocorrelation function for the object. The relationship between the sampling frequency in the detector plane (fixed by the detector pixel width Δ_d) and the sample plane is set by the discrete Fourier transform as $\Delta_d = \lambda Z/N\Delta_s$, where Z is the distance between the sample and detector planes. Therefore, the relationship among the maximum sample size that can be imaged, the wavelength, the sample-to-detector distance, and the detector pixel width is given as:

$$d < \frac{\lambda Z}{2\Delta_d} \qquad (4)$$

If this sampling requirement is met and the detector is located in the far field of the diffracting object, i.e., $d^2 \ll \lambda Z$, then the approximations of plane-wave CDI will, in general, hold.

An additional complication arises because the undiffracted zeroth-order component of the transmitted wave through the sample is normally many orders of magnitude brighter than the diffracted wave surrounding it. Since the smallest features that can be reconstructed in the object are limited by the bandwidth of the spatial frequencies measured at the detector, the upper limit on the spatial resolution of CDI is in most cases set by the maximum detection angle for the scattered photons. Hence, plane-wave CDI usually requires a beamstop to be placed at the detector in order to block the zeroth-order component. This has the unfortunate side effect of removing the low spatial frequency

information from the diffraction pattern. Miao et al.[31] originally solved this problem by using a low-resolution optical micrograph of the object to fill in the low spatial frequency information. Since low values of q correspond to larger features in the sample, low-resolution sample information is sufficient to fill in the missing information behind the beamstop. In cases where low-resolution *a priori* information about the sample is not available, a variety of solutions have been developed to try to determine the object support. One of the most useful tools is the so-called "shrink-wrap" algorithm where the weaker contributions to the reconstructed object transmission function are slowly removed with each iteration of the phase retrieval algorithm.[38] If applied with some caution, this approach can be used to accurately determine the final support for the sample in the absence of any additional *a priori* information. With a good guess at the sample outline, it is again possible to fill in the missing spatial frequencies due to the beamstop.

As noted by a number of authors previously, the reconstruction of real-valued objects is normally more straightforward than complex-valued objects, especially in the case where the size and shape of the sample profile are not accurately known (since this determines the support constraint).[33,39] However, real-valued objects must satisfy the requirements of being both physically thin and optically transparent, which will ensure that the ratio of the real and imaginary components of the sample refractive index is approximately unity such that the phase factor can be ignored. If these conditions are met, the recorded diffraction pattern will be centro-symmetric since $F(q) = F(-q)$. Samples that are binary or samples that are formed from one element and illuminated by hard x-rays are both cases where the resulting diffraction pattern should be centro-symmetric. For many samples, though, it can be a matter of practical difficulty to meet the requirements for centro-symmetric diffraction. In addition, recovery of the global phase information can sometimes provide vital additional insights into the material structure. Nonetheless there are published examples where centro-symmetry has been effectively applied, particularly for biological samples.[40]

Applications to Materials Imaging

Since the first demonstration of the plane-wave CDI method by Miao et al. in 1999[31] on a sample consisting of a series of gold nanodots deposited onto a silicon nitride membrane, the technique has found widespread application in the 2D and 3D imaging of materials science samples. The first buried structure was imaged in 3D in 2002, although the tomographic dataset only consisted of a relatively limited number of projections (30 in total).[41] In 2005, Chapman[36] convincingly demonstrated 3D plane-wave CDI on a test object composed of a pyramid of 50-nm gold

spheres. Semiconductor quantum dots have been reconstructed in 2D and 3D by Miao et al.,[42] and by collecting data above and below an absorption edge, the same group were later able to demonstrate specific elemental contrast enhancement on a buried structure.[43] In 2008, Barty et al.[44] were able to reconstruct the 3D structure of a ceramic nanofoam (Fig. 5). Another important breakthrough was the realization of CDI using table-top x-ray sources, which has been demonstrated at the sub-100-nm scale for gold test samples.[45,46] Finally the application of plane-wave CDI to imaging magnetic materials was reported by Turner et al.[47] in 2011 when they used polarized x-rays combined with plane-wave CDI for the high-resolution imaging of the magnetic domain structure (Fig. 6).

A major application and driver for the development of plane-wave CDI is the recent availability of x-ray free electron lasers (XFELs). These provide extremely bright femtosecond pulses of x-rays at the sample with peak brightness up to 9 orders of magnitude greater than at third-generation synchrotrons. The number of incident photons contained within a single XFEL pulse is so large that high-resolution diffraction information can be collected from samples with each femtosecond x-ray pulse. During a single pulse, nuclear motion in the sample may be neglected; however, the electronic structure of the sample will evolve eventually leading to a breakdown of the sample structure such that it is damaged or destroyed with each measurement.[48,49] This means that scanning methods cannot generally be applied at an XFEL unless the incident flux and thus diffraction resolution is reduced. Hence, plane-wave CDI is currently the
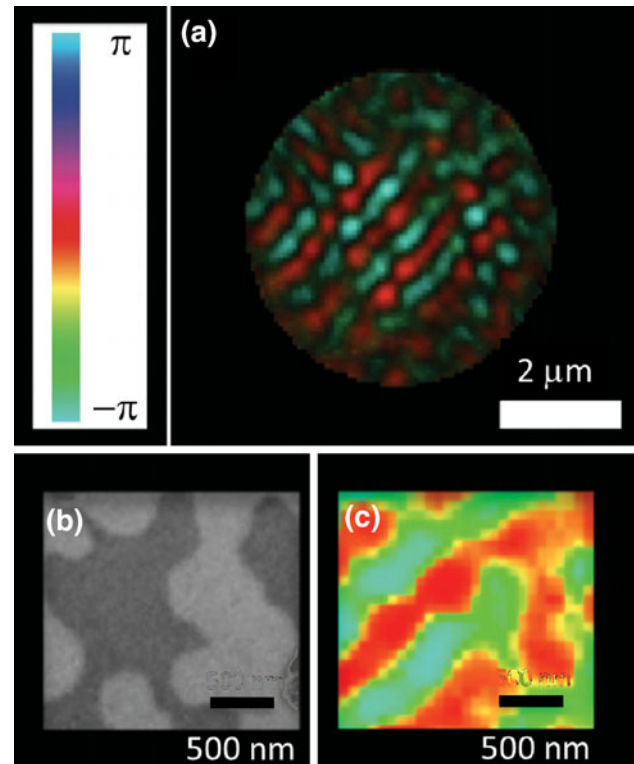

Fig. 6. (a) An image of magnetic domains in TbCo reconstructed by phase retrieval from the magnetic diffuse x-ray scattering with a spatial resolution of approximately 75 nm. Amplitude and phase of the complex image are shown as brightness and color, respectively. (b) A magnetic transmission x-ray microscopy (MTXM) image of the magnetic domain structure of a different region of the same sample at 22-nm spatial resolution. (c) A phase-only display of the reconstruction for the same field of view. (Reprinted with permission from Ref. 47, Copyright © 2011 by the American Physical Society.)
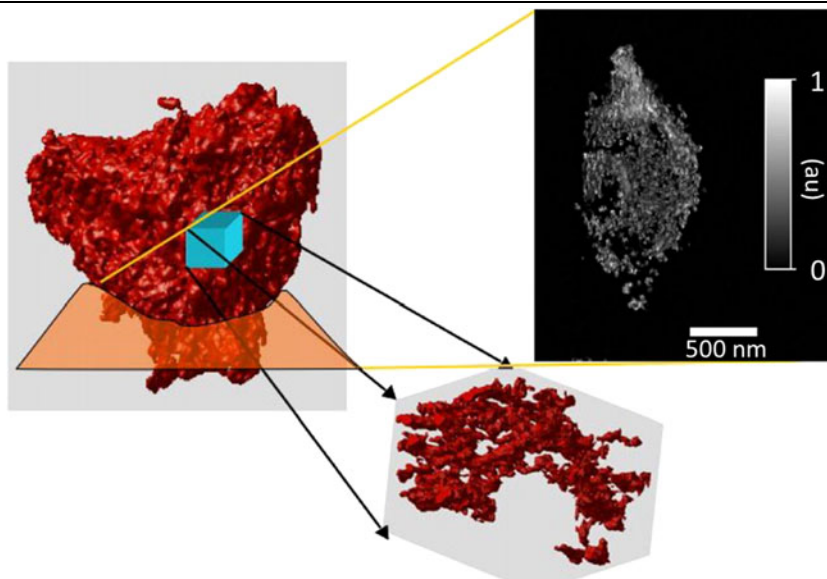

Fig. 5. Section and isosurface rendering of a 500-nm cube from the interior of the 3D volume of a ceramic nanofoam. The foam structure shows globular nodes that are interconnected by thin beamlike struts. (Reprinted with permission from Ref. 44, Copyright © 2008 by the American Physical Society.)

primary diffractive imaging method being applied at XFELs. Although XFEL plane-wave CDI is still in the early stages of development, the technique has already been used to image 2D test objects and to study nanospheres in flight using femtosecond XFEL pulses.[50]

PTYCHOGRAPHIC CDI

Basic Principle and Method

As described earlier, there are a number of conditions that must be met in order to apply plane-wave CDI. Some of the constraints on plane-wave CDI and in particular the requirement for a small isolated sample imposed by oversampling have been solved by the community through the development of alternative CDI techniques. One of the most successful of these methods has been that of ptychography. An early pioneer of ptychography was Walter Hoppe in the late 1960s and early 1970s when the method was originally developed for applications involving EM.[51] Although it was not widely taken up by the electron community, after the experimental demonstration of CDI in 1999[31] it has since been revisited in the context of x-ray phase retrieval techniques.

In ptychography, a small probe is scanned in a step-wise fashion relative to the sample, and at each overlapping probe position, the diffracted intensity is recorded (Table I, 3rd row). Once the entire region of interest within the extended sample has been imaged, the measurement is stopped. If the illuminating probe is small enough, the diffracted intensities are sufficiently large in comparison with the zeroth-order component that no beamstop is required. Hence, there is normally no loss of low-frequency information in ptychography. In place of the sample support constraint, an overlap constraint is applied, so that instead of the sample outline, one now needs to accurately determine the relative position on the sample at which each diffraction pattern was collected. A description of the ptychographic algorithm is provided by Faulkner and Rodenburg[52] The amount of illumination overlap required has been discussed in the literature, but in general greater than around 60% will produce an adequate reconstruction.[53] The motor encoder resolution, vibration, and sample drift can all introduce errors into the recorded positions at which diffraction patterns are collected. The wider inclusion of experimental techniques such as interferometry can greatly reduce the positioning errors; however, misalignments of even a few nanometers can have a critical influence on the resulting image. Much in the way that determining the sample support function has now been automated in plane-wave CDI, there has been rapid progress in "position-searching" algorithms that determine the actual illumination positions on the sample.[54] The development of these automated position searching algorithms has been of enormous benefit to the

practical implementation of ptychography, and the technique has now emerged as one of the mainstays of the CDI community.

In standard implementations of plane-wave CDI, the reconstructed phase of complex transmission functions is not quantitative in the sense that the incident plane wave is not measured and so does not provide a definite phase offset. In ptychography, however, the illumination function is reconstructed along with the sample ESW. This has the important benefit that the phase of the object is reconstructed relative to the phase of the complex illumination function. This means that it is possible to extract quantitative information about the sample.[55] For example, if the sample thickness is known, it is possible to obtain an estimate of the complex refractive index or if the sample's optical properties are well characterized, the reconstructed phase can yield the sample thickness.[56]

Applications to Materials Imaging

Phase retrieval using ptychographic CDI was first demonstrated using hard x-rays by Rodenburg[57] in 2007 using a random distribution of gold spheres ranging from 0.25 μm to 1.5 μm in diameter. The method has since been demonstrated for a large number of materials samples including the 2D imaging of buried nanostructures[58] and 3D tomographic imaging of the microstructure of hardened cement.[59] The potential of the technique for biological specimens was demonstrated in 2010 when Dierolf et al.[4] published a ptychographic reconstruction of part of the mouse femur at a spatial resolution of 100 nm. By measuring ptychographic CDI data at two different photon energies below the Au L_3 absorption edge (11.920 keV), Takahashi et al.[60] have claimed to observe an increased sensitivity to the elemental distribution within Au/Ag nanoparticles (Fig. 7). Ptychography has also been applied to the extraction of the magnetic domain structure using polarized x-rays in 2011 by Tripathi et al.[61] Finally, just as with scanning transmission x-ray microscopy, the small probe size also lends itself to combination with fluorescence detection, which has been demonstrated by Schropp et al.[62] for the imaging of a nanostructured microchip.

DIVERGING BEAM CDI

Basic Principle and Method

In parallel to the development of ptychographic methods has been the realization of CDI techniques using an illumination with a known phase structure. One of the most successful implementations of these types of methods has been Fresnel coherent diffractive imaging (FCDI), in which a phase curved illumination is used to illuminate the sample.[63] The theoretical basis for this technique stems from the work of Nugent et al.[64] in considering phase retrieval via the transport of an intensity equation.
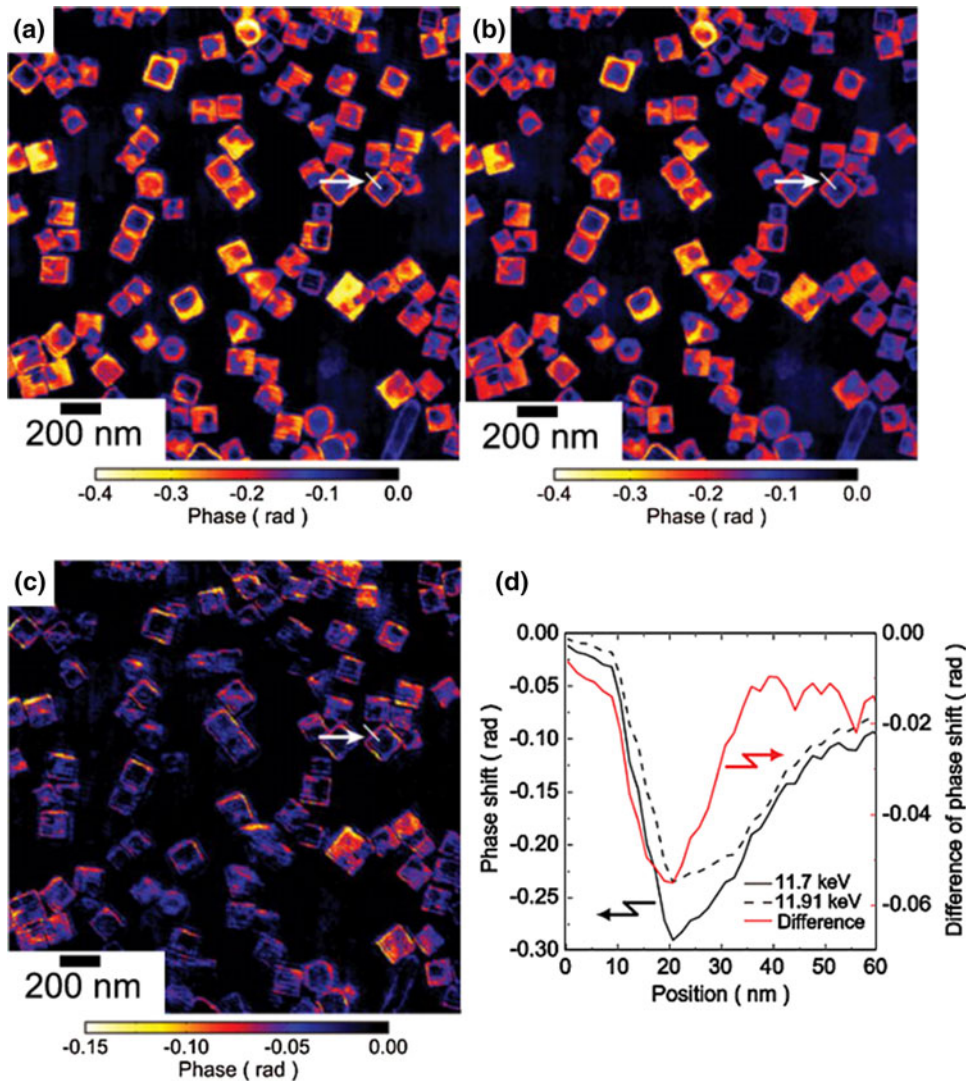
Fig. 7. Reconstructed phase maps of the Au/Ag nanoparticles at (a) 11.7 keV and (b) 11.91 keV (the Au L$_3$ edge is at 11.920 keV). The pixel size is 8.4 nm. The total number of pixels is 300 × 300. (c) Difference image of the phase maps at 11.7 keV and 11.91 keV. (d) Cross sections through the white lines in (a)–(c). (Reprinted with permission from Ref. 60, Copyright © 2011 by the American Institute of Physics.)

It was later argued that the use of a curved incident illumination would overcome many of the convergence issues of plane-wave CDI, particularly for complex objects.[65–67] In particular, the translational invariance of plane-wave CDI results in "trivial ambiguities" identified by Bates[68] as a transverse spatial shift, a constant additional phase, and a complex conjugation that can prevent convergence. It has been shown that in FCDI these ambiguities do not exist,[69] resulting in rapid and robust convergence of the algorithm.

In FCDI, a curved beam, normally generated by a Fresnel zone plate (FZP), is used to illuminate the sample (Table I, 4th row). The oversampling and far-field condition for the sample still need to be met, but due to the beam divergence, the holographic region formed from interference between the incident illumination and the sample ESW is visible on the detector. It is important to realize that

FCDI is a two-part experiment. In the first part, the complex wave illuminating the object must be determined in order to allow its features to be separated from that of the complex sample ESW, which is recovered in the second part.

The determination of the phase of the illuminating wave-field at the detector is achieved using the method of Quiney et al.[70] This method was derived in the context of a FZP, although we note that CDI has also been used by Kewish et al.[71] to phase the diverging beam produced from a pair of Kirkpatrick–Baez mirrors. With knowledge of the illumination intensity at the detector, the extent of the pupil function as well as the focal length and focus-to-detector distance, CDI phasing algorithms can be employed incorporating the appropriate prefactor to the integral and spherical phase factor within the integrand defining the Fourier transform of the pupil ESW. Both factors depend on the reciprocal of

the distance from the sample to detector, z_{sd}, such that in the limit that z_{sd} becomes large these factors can be neglected and we recover the direct Fourier transform used in the propagation for plane-wave CDI. Performing a three-plane propagation, i.e., lens to focus to detector, enforcing the modulus constraint in the detector plane and the support function of the lens in the pupil plane leads to recovery of the complex illumination function.

Assuming the complex illumination function has been accurately determined, the second half of the experiment involves reconstructing the complex sample transmission function. In this part of the experiment, the sample ESW is propagated between the sample and detector planes only (two plane propagation). For the interested reader, a practical guide to FCDI is given by Williams et al.[72]; however, it is worth noting here that in FCDI, unlike plane-wave CDI, the illumination is subtracted at the detector plane to allow the support constraint to be effectively applied in the sample plane.

The spatial resolution of FCDI is identical to all other forms of CDI in that the theoretical upper limit is generally set by the angle to which the diffracted photons are detected. Phasing the diffraction within and up to the numerical aperture (NA) of the FZP provides a maximum resolution equal to the size of the focal spot. Diffraction outside of the NA of the FZP increases the resolution of the reconstructed image beyond that of the FZP until the outermost fringes are phased. Because the illumination is reconstructed separately, the sample ESW is recovered relative to the incident illumination (similar to ptychography), and the technique is thus quantitative. In addition, the use of an FZP to form the curved incident beam means that the zeroth order is blocked in the pupil plane rather than at the detector; hence, there is no loss of low spatial frequency information.

An important development in FCDI occurred in 2008 when it was first demonstrated that the edges of the curved illumination on the sample could be used to define the support function for the sample.[73] This approach, known as Keyhole CDI, permits the reconstruction of regions of interest within extended samples without any need for scanning. With improvements in detector technologies and in particular photon counting detectors as well as the development of XFELs, this opens up the possibility of conducting time-resolved measurements.

Applications to Materials Imaging

The first experimental demonstration of FCDI was due to Williams et al. In this work, the curved-beam diffraction pattern collected from a gold chevron nanostructure was phased.[63] The resolution of the reconstructed sample was 24 nm, a factor of two improvement over the maximum theoretical resolution of the FZP used to illuminate the sample. The inherent quantitative nature of FCDI was

demonstrated by Clark,[74] using the reconstructed phase of the sample ESW for gold nanostructures. Keyhole CDI at a spatial resolution below 20 nm was shown using an Xradia resolution target.[73] In 2008, Keyhole CDI was carried out on an integrated circuit (Fig. 8) by Abbey et al.[75] In this study, the void fractions in the interconnect regions were determined through analysis of the phase advance within this region compared with the surrounding fuse.

Using ptychographic methods, Vine et al.[76] were able to demonstrate that ptychographic FCDI retains many of the advantages of ptychography while requiring far less data and with less stringent requirements on the amount of overlap required. This was extended to include diffraction measurements recorded at multiple defocus positions by Putkunz et al.[77] to improve the quality and reduce the required x-ray dose for FCDI. Tomography using FCDI has been experimentally demonstrated using both visible light[78] and x-rays[79] on a lithographed glass test object.

CDI WITH PARTIAL COHERENCE

Basic Principle and Method

Frequently, in materials science, imaging over length scales of 10's of microns or more is required. Sampling considerations are one barrier to CDI being applied over these lengths scales. Another major issue, particularly at higher energies, is coherence. Spence et al.,[80] Robinson et al.,[81] and Vartanyants and Robinson[82] are among the authors to discuss the coherence requirements for diffractive imaging. In the following, we first consider spatial coherence since this is normally the more critical parameter at synchrotron sources. In crystalline diffraction, as the coherence length becomes shorter, the Bragg diffraction peaks broaden and begin to overlap such that the intensities between them are no longer zero. Similarly, in a continuous diffraction pattern, reducing the coherence results in the intensity values at the diffraction minima increasing relative to the maxima. From a simple perspective, when the coherence length is reduced such that this increase in the intensity at the minima of the diffraction pattern becomes detectable, the standard imposition of the Fourier modulus constraint in the diffraction plane is incorrect. Even a small blurring of the diffraction intensities due to a reduced spatial coherence length can have a critical effect on the object reconstruction, changing the redistribution of the reconstructed amplitude or preventing convergence all together. If the spatial coherence length continues to be reduced, eventually it becomes no longer possible to detect the location of the diffraction minima due to blurring and the information is essentially lost in the measurement.

Spence et al.[80] argue that for CDI to be applied effectively, the spatial coherence length at the
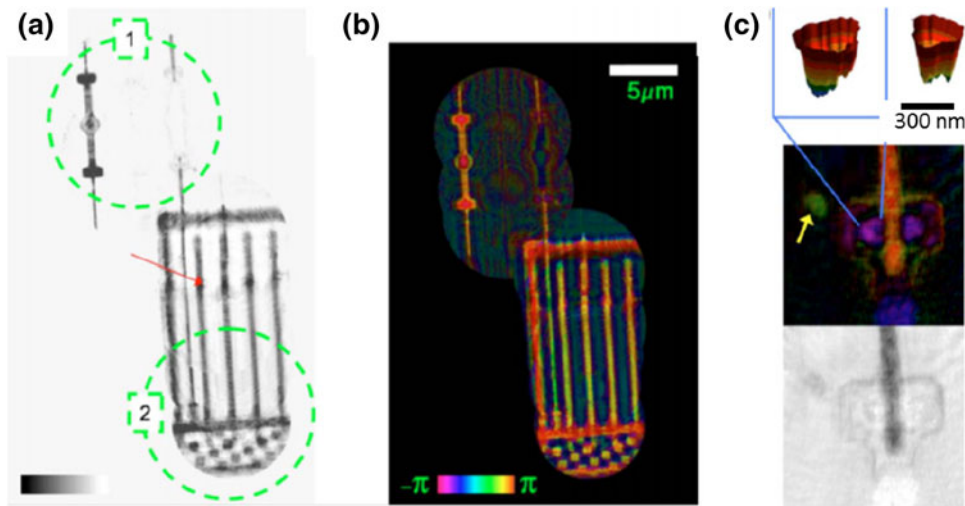
Fig. 8. (a) 2D CDI image of the transmission $T(\vec{r})$ amplitude comprising ten independent reconstructions. The arrow indicates the boundary between thin and thick regions of the sample. The two areas circled in green are regions where the scan was paused to increase the amount of detected scatter at high angle, resulting in a higher resolution image. (b) The reconstructed sample ESW, with the brightness representing the amplitude and the color representing the phase. (c) Reconstruction of void defects in Ta liner. Top row: 3D graphs based on phase difference through voids compared with the surrounding Ta liner. (Reprinted with permission from Ref. 75, Copyright © 2008 by the American Institute of Physics.)

sample should be equal to the width of its autocorrelation since the sampling theorem implies that the oversampled diffraction pattern contains information across this entire region; i.e., $l_c^{sp} \geq 2d$ (recall that d is the sample diameter). Typical coherence lengths for hard x-ray beamlines at third-generation synchrotron facilities (e.g., ESRF, APS, and SPRING-8) are of the order of microns.[83] This places tight constraints on the size of sample that can effectively be recovered using plane-wave CDI. The issue of partial spatial coherence in CDI is a critical one, and approaches that incorporate partial coherence in the phase retrieval of the diffracted wave have been developed to compensate for this. These methods assume a quasi-monochromatic field and rely on the modal decomposition of the mutual optical intensity (MOI) $J(r_1, r_2)$ into a sum of coherent modes $\psi(r)$, which are mutually incoherent; i.e.,

$$J(r_1, r_2) = \sum_{n=1}^{N} \mu_n \psi_n(r_1) \psi_n^*(r_2) \qquad (5)$$

where μ_n are positive real numbers that determine the occupancies of the modes.[84] Experimentally determining the exact form of $\psi(r)$ is challenging, although it has been demonstrated by Flewett et al.[85] based on a MOI experimentally measured using phase space tomography by Tran et al.[86] In practice it has been shown that for a synchrotron undulator source, $J(r_1, r_2)$ is well approximated by the product of 1D Gaussian Schell model functions. Furthermore, it has been shown in experimental diffractive imaging studies that $J(r_1, r_2)$ only needs to be considered over distances less than the furthest separation of scattering centers within the sample such that just a few coherent modes are

needed in the propagation of the partially coherent sample ESW. Knowing this we can choose a set of basis functions for ψ_n that conveniently represent the first few coherent modes of the Gaussian Schell model that were determined by Starikov and Wolf.[87] In 2009, Whitehead et al.[88] were able to apply these ideas to plane-wave CDI demonstrating significant improvements in the convergence and quality of reconstruction obtained by including a priori knowledge of the beam coherence properties in the propagation. The limits on the degree of partial coherence that can be tolerated, using a priori information about the coherence properties of the source, is discussed in a recent publication.[89]

An interesting development has been the use of the partially coherent modal propagation framework to solve problems where the measured diffraction signal is made up of a statistical ensemble of different states or configurations of the sample. Instead of having to account for fluctuations in the degree of correlation between different points on the wavefront, this idea transfers the "partially coherent" characteristics of the experiment to the sample rather than to the source. Quiney and Nugent[90] first proposed this use of the partial coherence formulism to extract the molecular structure from single-molecule diffraction data, which necessarily contains a continuum distribution of molecular configurations and electronic states. In another paper by Dilanian et al.,[91] the same formulism was applied to fitting the continuous diffraction from imperfect nanocrystals in order to recover their structure factors. These ideas were recently further explored in the context of ptychography by Thibault and Menzel.[92]

For temporal coherence, the bandwidth of most monochromators is sufficiently narrow that even for

the high-resolution images obtained in CDI, the effects of a finite temporal coherence length are not detectable. Effectively partial temporal coherence reduces the bandwidth of the useable signal collected at the detector lowering the resolution of the resulting reconstruction. In terms of the maximum scattering angle detected, the temporal coherence length $l_c^{tm} > 2d\theta_{max}$ for CDI to be applied at the maximum possible resolution. This inequality can be more conveniently be rewritten in terms of the x-ray energy as $E/\delta E > 2d\theta_{max}/\lambda$.

In the case of table-top high-harmonic generation (HHG) x-ray sources, temporal coherence can be an important issue since to make use of all of the available flux it may be necessary to consider a spectral distribution that cannot be represented by a single optical mode.[93] In 2009, Chen et al.[94] were able to demonstrate CDI with a HHG source using a method that included information about the experimentally determined spectral distribution. In this case, the spectrum consisted of six distinct and well-separated harmonics, each one of which was narrow enough that it could be represented by a single wavelength. A separate ESW for each sampled wavelength was propagated and combined at the detector according to their spectral weighting. A single component corresponding to just the central wavelength was then extracted and propagated back to the sample plane where the usual support constraint was applied and the estimate of the sample transmission function updated. This idea was further developed for synchrotron undulator sources that have a continuous spectral distribution requiring a finer sampling.[95] In this case, only the ESW corresponding to the central wavelength was propagated in either direction with weighting, summing, and interpolation of the diffraction patterns according to their wavelength-dependent spatial frequencies all occurring in the detector plane. The limit on the bandwidth that can be tolerated using this technique, derived on basis of the visibility of the interference function between the two most closely spaced scattering centers within the sample, has been discussed in the literature.[95]

The field of partially CDI is still in its early stages of development as such the only experimental applications reported to date have been for fabricated test objects; hence, we omit the "applications to materials imaging" section here. Nonetheless it seems clear that we have only begun to scratch the surface of the potential offered by the partial coherence formulism for CDI in the context of materials characterization.

COHERENT X-RAY MICROBEAM DIFFRACTION

Basic Principle and Method

The techniques discussed so far have been carried out largely in the absence of any significant defects or strain. The remainder of this review is devoted to the discussion of x-ray techniques that can be used to characterize individual dislocations and their associated structures. Imaging a highly perfect crystal via the 2D detection of x-rays diffracted from its constituent lattice planes, known as x-ray diffraction topography (XRT), has been employed since the 1930s.[96] Early contributors to the XRT field include such famous luminaries as Berg,[96] Barrett,[97] Guinier and Tennevin,[98] and Lang.[99] There are no specific coherence requirements as such for XRT, and it was initially demonstrated using lab-based sources. However, it is useful to provide a brief description here since it clarifies the motivation for the development of the techniques described in the remainder of this review.

XRT has the capability of imaging single dislocations over large areas and is used routinely for defect imaging—particularly as a means of quality control. XRT principally relies on diffraction contrast formed from the interference of waves inside the crystal allowing for the visualization of individual crystallographic line defects (dislocations) and local lattice strains. The strain sensitivity of XRT has been quoted as approaching $(\Delta l)/l \sim 10^{-8}$ (where Δl is the relative change in the lattice spacing). Due to the high spatial resolution of modern detectors, features approaching $1\ \mu m$ can be resolved within areas as large as $100\ cm^2$. For a comprehensive summary of the current state-of-the-art of XRT, the NIST review by Black and Long[100] provides an excellent reference.

Plastic deformation of metallic crystals is mediated by the formation and propagation of dislocations that self-organize into "hard" dislocation-rich walls enclosing "soft" regions of low dislocation density (cells). This dislocation patterning has profound consequences for material hardening and failure. However, because of lattice rotation between cells, ray-tracing from the diffraction image to the sample required for topography is not possible. This intrinsic problem of real and reciprocal space convolution has previously prevented XRT from being used to image the deformation structure within (poly) crystals. There has been some attempt to try to optimize both XRT and DCT for the quantitative determination of lattice misorientations via a technique known as reticulography in which the sample is placed in the Laue configuration and a fine absorbing mesh is placed between the sample and the detector. However, this still does not permit the examination of highly deformed samples and the ultimate resolution is still detector limited.

In terms of advancing our fundamental understanding of materials deformation, one of the most important developments in x-ray studies of materials science samples has been the development of micro and nanofocused beams of hard x-rays. Reducing the size of the incident beam to the point where the cumulative amount of lattice curvature within the sampling volume is sufficiently small that the Bragg reflection is well defined is perhaps

the simplest way of deconvolving real and reciprocal space information. This approach does not require any phasing of the diffraction pattern, and provided the incident beam is smaller than the length scale of the dislocation cells, the lattice rotation gradient and FWHM of the Bragg reflection provides a means of distinguishing between the individual cell walls and their ordered interiors.

An example of the dramatic difference between the information that can be obtained depending on beamsize is illustrated in Fig. 9, which shows the Bragg reflection from a single Ni grain with a 0.1-mm^2 beam and a 600 μm^2 beam.[7,101] With the larger beam, which illuminates the entire grain, lattice rotations within the grain prevent any real-space interpretation of the diffraction data. With the submicron beam, the Bragg reflection closely resembles the incident illumination, and when the small probe is scanned across the sample, it is simple to relate the features of the Bragg reflection to the real-space position on the sample.

Using micro and nanodiffraction, it is possible to study plasticity effects at the level of single dislocations in bulk materials where EM techniques cannot be applied. Hence, because of the rapid improvement of the resolution of x-ray optics, increasingly x-rays are becoming a viable option for materials studies at the highest resolutions. This is providing researchers with a wealth of new information about defect behavior within materials of length scales significantly larger than a micron that both complements and challenges some of the results from the huge body of EM work carried out on thin samples and nanocrystals.

Applications to Materials Imaging

There are now a number of examples of coherent x-ray microbeam diffraction being used to study single dislocations and dislocation networks. In 2007, Ravy et al.[102] analyzed microdiffraction data from $SrTiO_3$ and were able to spatially disentangle the short and long length-scale components, the latter being attributed to static ordered domains. In 2011, the dislocation substructure in deformed polycrystalline Ni, shown in Fig. 10, was mapped using microbeam diffraction.[7] From analysis of the diffraction patterns, the researchers found that with
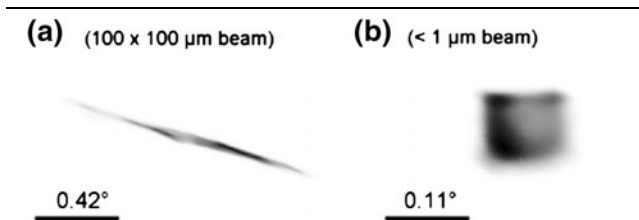
increasing applied load, more dislocations were trapped in thinner regions of the grain. It was concluded that this must be due to size effects influencing the subgrain deformation structure; the variation of defect density with size was found to follow a power law similar to that of the Hall–Petch effect or ordinary dislocation plasticity. It is interesting to note that this is the reverse of observations made in single crystals, e.g., in nano-indentation experiments made on pillars.[103]

In another study, Jacques et al.[104] used micro-beam coherent x-ray diffraction to examine the dissociation of a single bulk dislocation in silicon. Their work revealed a larger distance between the partials than had previously been observed in similar studies performed with TEM on thin films, again highlighting the dramatic differences in defect behavior across the length scales.

BRAGG COHERENT DIFFRACTIVE IMAGING (BCDI)

Basic Principle and Method

Examining the changes in the Bragg reflection structure over the entire rocking curve can yield a wealth of detailed structural information compared with looking at information from a single diffraction angle alone. Before the first demonstration of CDI, researchers were using the technique of reciprocal space mapping (RSM) to collect as much information about the diffracting sample as possible.[105] RSM involves the collection of Bragg reflections on the crystal rocking curve at very high angular resolution. RSM shares many common characteristics with the last technique we will discuss in this review, that of BCDI. For an in-depth discussion of this technique, further information can be found in articles by Harder and Robinson within this issue of *JOM*.

A 3D crystal lattice will have a 3D lattice in reciprocal space, a plane of atoms in a crystal will create a line in reciprocal space, and a perfect 3D
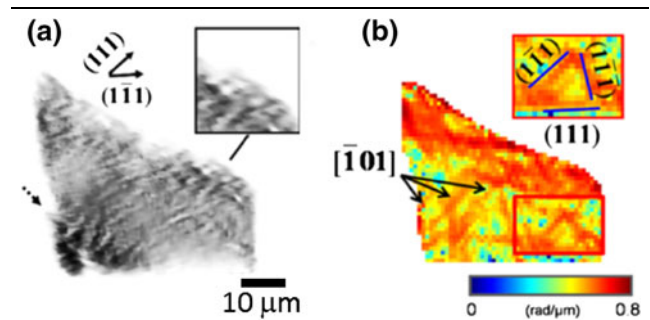

Fig. 10. Microdiffraction data showing a subgrain structure in polycrystalline Ni (a) composite of 5041 Bragg reflection intensities showing the whole grain. (b) Lattice rotation gradient in the diffraction angle after final loading to 4% plastic strain. The width of the dislocation cell walls is between 1 μm and 2 μm, and their separation is typically 4–10 μm. (Reprinted with permission from Ref. 7, Copyright © 2011 by Elsevier.)

Fig. 9. Bragg reflections from a single grain in a Ni polycrystal using (a) 100 × 100 μm incident illumination and (b) a 0.06 × 0.06 μm incident illumination. (Reprinted with permission from Ref. 7, Copyright © 2011 by Elsevier.)

array of atoms will create a single spot in reciprocal space. Information about the "average" characteristics of the crystal lattice is contained close to the origin of this spot, whereas the detailed structure is contained in the areas further out from the origin. The size and shape of the reciprocal lattice spot (Bragg spot) contains information about the dimensions of the diffracting volume, and if there are defects or distortions in the crystal lattice, there will be other length scales that alter the position, shape, and intensity distribution around the reciprocal lattice point.

The intensity distribution of a single Bragg spot may thus be attributed to the crystal electron density $\rho(r)$, the "shape function" $s(r)$, which is related to the diffracting volume and the relative displacements of the atoms from their ideal lattice positions $u(r)$:

$$I(q) \propto \left| \int_0^\infty \rho_{\mathrm{L}}(r)s(r)\mathrm{e}^{iq.r}\mathrm{e}^{iq.u(r)}\mathrm{d}r \right|^2 \qquad (6)$$

Typical strain sensitivities quoted in the literature for BCDI are of the order of $(\Delta l)/l \sim 10^{-4}$.[13] When the crystalline lattice is completely strain free, i.e., $u(r) = 0$, the intensity depends only on the modulus of the Fourier transform of a purely real shape function. Thus, the diffraction pattern around each Bragg reflection will be identical and centro symmetric. With the introduction of strain into the lattice, the shape function will become complex since now $s(r) = |s(r)|\mathrm{e}^{iu(r).q}$; therefore, the problem of reconstructing the real-space crystal lattice becomes one of retrieving the phase for a complex object.

It was Robinson and Vartanyants who first applied the ideas about CDI and oversampling as a method of phase retrieval to the problem of retrieving the phase of the continuous diffraction pattern around a Bragg spot[106] They realized that the same principles used to recover phase information in the plane-wave CDI case could be applied to recovering the phase of a single oversampled Bragg reflection. The initial demonstration applied to Au nanocrystals assumed a perfect crystalline lattice, ignoring the imaginary part of the real-space density.[106] Using CDI in Bragg reflection geometry, they were able to demonstrate the reconstruction of the 2D projected shape of the Au nanocrystals from a single oversampled Bragg reflection. These ideas were later extended to the reconstruction of arrays of quantum dots, and a theoretical framework for the effects of partial coherence in BCDI was also published.[82] In 2006, the first reconstruction of the 3D deformation field within a lead nanocrystal was published by Pfeifer et al.[107] by collecting high-resolution Bragg diffraction data in finely spaced increments along the nanocrystal rocking curve. There has since been rapid progress in the field of BCDI, most notably, the combination of BCDI with ptychography in projection and in 3D, with a full rocking curve collected at each point in the ptychographic scan.[108] Also, a

recent paper by Clark et al.[109] demonstrated the inclusion of a 3D partially coherent wave propagation in BCDI with dramatic improvements in the quality of the reconstructions.

Applications to Materials Imaging

BCDI is ideally suited to applications involving materials science samples. The resolution of the reconstructed crystal shape and internal deformation field depends on the area of reciprocal space covered by the scattering signal around the individual Bragg spots. The x-ray scattering power of most materials science samples is relatively strong; hence, these samples give the best signal for CDI. The highest resolution reported so far for BCDI was for the reconstruction of Au nanoparticles using a nanofocused incident beam where 5 nm spatial resolutions was achieved.[56] An important result published by Newton et al.[110] was the recovery of the 3D strain tensor within a ZnO nanorod based on reconstruction of the atomic displacements along the three principal axes from measurements of six independent reflections. BCDI has also been used for the analysis of stacking faults in InAs/InP and GaAs/GaP nanowires through model matching.[111] Bragg ptychography using a FZP nanofocused beam has allowed the characterization of lattice strains in a multilayer semiconductor device.[112] A recent result that has been reported by Takahashi et al.[113] is the reconstruction of the deformation field due to a single dislocation in a bulk silicon crystal using Bragg ptychography (Fig. 11). This result paves the way for 3D quantitative characterization of dislocations in the bulk that is expected to have important implications for addressing gaps in our knowledge over the important 1–10-μm range where size effects are known to persist.

SUMMARY AND CONCLUSIONS

Since its earliest origins, x-ray science has showed great promise for imaging materials science samples and it is surprising to think that techniques such as x-ray topography allowed the visualization of crystallographic defects as early as the 1940s. With the development of third- and more recently fourth-generation x-ray sources as well as the huge advances in x-ray detector technology that have been made, we are now seeing some truly remarkable results from the x-ray microscopy materials science community. The coherent output of modern synchrotron sources combined with the high-resolution and sensitive detection of scattered x-rays is providing new types of data that have directly enabled the realization of techniques such as CDI. The coherent methods discussed in this review can now be considered to be largely matured, although there is still some development needed of key aspects. For example, although 3D Bragg-ptychography has been demonstrated, there is still much work to be done both in improving the experimental
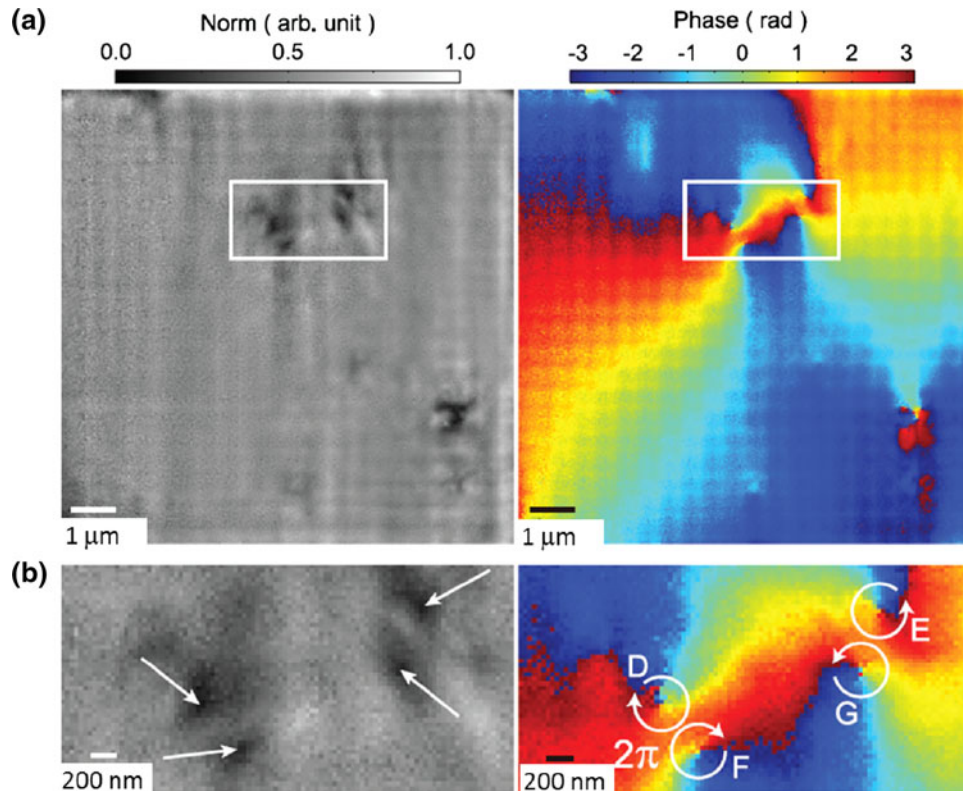
Fig. 11. (a) Norm (left) and phase (right) maps of the locally averaged local crystal structure factor reconstructed from Bragg ptychography diffraction patterns. The pixel size is 35.4 nm, and the total number of pixels is 294 × 294. (b) Enlarged norm and phase maps of the area indicated by the square in (a). (Reprinted with permission from Ref. 113, Copyright © 2013 by the American Institute of Physics.)

set up and in developing optimization algorithms for aligning the 3D reciprocal volume data.

The techniques discussed in this review (summarized in Table I) cover almost all length scales of relevance to fundamental materials science, ranging from the 3D reconstruction of grain boundary networks using PCT to the quantitative imaging of single defects in the bulk using BCDI. The development of *in situ* TEM deformation experiments led to significant advances in our fundamental understanding of materials behavior. 3D x-ray imaging at the nanoscale is promising a similar impact for bulk materials characterization. However, spatial resolution is only one issue and is an area that, with the development of techniques such as CDI, is already being addressed. One of the focus areas in the next stage of coherent x-ray development will be on combining this high spatial resolution with time resolution to enable one to the study of dynamical processes. With the increasing availability of fast-readout, photon counting detectors, the time-resolved acquisition of diffraction data with sufficient statistics to enable reconstruction of the sample is feasible. Techniques such as plane-wave CDI, Keyhole and FCDI, as well as BCDI are all amenable to time-resolved studies. The recent availability of XFELs also offers a huge range of possibilities for coherent imaging of materials undergoing ultrafast transitions and femtosecond snapshots of phonon

dynamics[114] and melting processes[115] have already been demonstrated. The implications of the realization of partially coherent diffraction microscopy are also only just being explored. With detailed knowledge of the coherence properties of the source, an illumination spot larger than the spatial coherence length of the beam can be used. Depending on the *a priori* knowledge available, other types of statistical averaging problems can also be addressed. Two applications, biomolecular imaging and disordered crystals, have been discussed in this review; however, there are certain to be many more. Broadband lensless imaging is also rapidly growing in usage. Not only does including a knowledge of the spectral distribution of the source enable the more efficient use of a wider variety of sources, but it also offers the possibility of resonant imaging studies in the future.

With the practical improvements in the quality and speed with which the coherent methods that have been discussed can now be applied, the shifting focus of research is increasingly on identifying key problems within materials imaging that these new techniques can address. CDI in particular has undergone extremely intensive development over the past decade and the current-state-of-the-art permits the high-quality reconstruction of materials science samples at spatial resolutions of 10's of nm with comparative ease. With the recent break-

throughs in the quantitative characterization of defects in bulk materials using CDI and with XFELs only a few years into their operation, we are just at the beginning of a new chapter in the high-resolution coherent x-ray imaging of materials. I hope that this review goes some way toward capturing the enormous progress that has been made in the field of coherent x-ray imaging in recent years and that it will serve as a useful guide to those wishing to use coherent x-rays as a means of investigating materials science problems.

OPEN ACCESS

REFERENCES

1. H.P. Klug and L.E. Alexander, *X-Ray Diffraction Procedures: For Polycrystalline and Amorphous Materials*, 2nd ed. (New York: Wiley, 1974).
2. B.P. Flannery, H.W. Deckman, W.G. Roberge, and K.L. D'amico, *Science* 237, 1439 (1987).
3. A.M. Korsunsky, N. Baimpas, X. Song, J. Belnoue, F. Hofmann, B. Abbey, M. Xie, J. Andrieux, T. Buslaps, and T.K. Neo, *Acta Mater.* 59, 2501 (2011).
4. M. Dierolf, A. Menzel, P. Thibault, P. Schneider, C.M. Kewish, R. Wepf, O. Bunk, and F. Pfeiffer, *Nature* 467, 436 (2010).
5. W.D. Nix and H. Gao, *J. Mech. Phys. Solids* 46, 411 (1998).
6. N.A. Fleck, *Acta Metall.* 42, 475 (1993).
7. B. Abbey, F. Hofmann, J. Belnoue, A. Rack, R. Tucoulou, G. Hughes, S. Eve, and A.M. Korsunsky, *Scr. Mater.* 64, 884 (2011).
8. H.D. Espinosa and B.C. Prorok, *J. Mater. Sci.* 38, 4125 (2003).
9. R.-M. Keller, S.P. Baker, and E. Arzt, *J. Mater. Res.* 13, 1307 (1998).
10. T.C. Lee, I.M. Robertson, and H.K. Birnbaum, *Philos. Mag. A* 62, 131 (1990).
11. A. Snigirev, I. Snigireva, V. Kohn, S. Kuznetsov, and I. Schelokov, *Rev. Sci. Instrum.* 66, 5486 (1995).
12. B.C. Larson, W. Yang, G.E. Ice, J.D. Budai, and J.Z. Tischler, *Nature* 415, 887 (2002).
13. R. Harder, M. Liang, Y. Sun, Y. Xia, and I.K. Robinson, *New J. Phys.* 12, 035019 (2010).
14. K.A. Nugent, *Adv. Phys.* 59, 1 (2010).
15. P. Cloetens, W. Ludwig, E. Boller, L. Helfen, L. Salvo, R. Mache, and M. Schlenker, *Proc. SPIE* 4503, 82 (2002).
16. A. Pogany, D. Gao, and S.W. Wilkins, *Rev. Sci. Instrum.* 68, 2774 (1997).
17. P. Cloetens (Ph.D. thesis, Vrije Universiteit Brussel, 1999).
18. J. Guigay, *Optik* 49, 121 (1977).
19. J.P. Guigay, *Opt. Acta: Int. J. Opt.* 18, 677 (1971).
20. A. Barty, K.A. Nugent, D. Paganin, and A. Roberts, *Opt. Lett.* 23, 817 (1998).
21. W. Ludwig, A. King, M. Herbig, P. Reischig, J. Marrow, L. Babout, E.M. Lauridsen, H. Proudhon, and J.Y. Buffière, *JOM* 62 (12), 22 (2010).
22. A. King, G. Johnson, D. Engelberg, W. Ludwig, and J. Marrow, *Science* 321, 382 (2008).
23. W. Ludwig, S. Schmidt, E.M. Lauridsen, and H.F. Poulsen, *J. Appl. Crystallogr.* 41, 302 (2008).
24. P. Cloetens, M. Pateyron-Salome, J.Y. Buffiere, G. Peix, J. Baruchel, F. Peyrin, and M. Schlenker, *J. Appl. Phys.* 81, 5878 (1997).
25. C. Antoine, P. Nygård, Ø.W. Gregersen, R. Holmstad, T. Weitkamp, and C. Rau, *Nucl. Instrum. Methods Phys. Res. A* 490, 392 (2002).
26. J. Baruchel, J.-Y. Buffiere, P. Cloetens, M. Di Michiel, E. Ferrie, W. Ludwig, E. Maire, and L. Salvo, *Scr. Mater.* 55, 41 (2006).
27. J.Y. Buffière, E. Maire, P. Cloetens, G. Lormand, and R. Fougères, *Acta Mater.* 47, 1613 (1999).
28. J.Y. Buffiere, E. Maire, C. Verdu, P. Cloetens, M. Pateyron, G. Peix, and J. Baruchel, *Mater. Sci. Eng. A* 234–236, 633 (1997).
29. D. Bernard, D. Gendron, J.-M. Heintz, S. Bordère, and J. Etourneau, *Acta Mater.* 53, 121 (2005).
30. Y. Wang, X. Liu, K.-S. Im, W.-K. Lee, J. Wang, K. Fezzaa, D.L.S. Hung, and J.R. Winkelman, *Nat. Phys.* 4, 305 (2008).
31. J. Miao, P. Charalambous, J. Kirz, and D. Sayre, *Nature* 400, 342 (1999).
32. D. Sayre, *Acta Crystallogr.* 5, 843 (1952).
33. J.R. Fienup, *J. Opt. Soc. Am. A* 4, 118 (1987).
34. R.W. Gerchberg and O. Saxton, *Optik* 35, 237 (1972).
35. V. Elser, *J. Opt. Soc. Am. A* 20, 40 (2003).
36. H.N. Chapman, *J. Opt. Soc. Am. A* 23, 1179 (2006).
37. S. Marchesini, *Rev. Sci. Instrum.* 78, 011301 (2007).
38. S. Marchesini, H. He, H.N. Chapman, S.P. Hau-Riege, A. Noy, M.R. Howells, U. Weierstall, and J.C.H. Spence, *Phys. Rev. B* 68, 140101 (2003).
39. J.R. Fienup, *Appl. Opt.* 21, 2758 (1982).
40. C. Song, H. Jiang, A. Mancuso, B. Amirbekian, L. Peng, R. Sun, S.S. Shah, Z.H. Zhou, T. Ishikawa, and J. Miao, *Phys. Rev. Lett.* 101, 158101 (2008).
41. J. Miao, T. Ishikawa, B. Johnson, E.H. Anderson, B. Lai, and K.O. Hodgson, *Phys. Rev. Lett.* 89, 088303 (2002).
42. J. Miao, C.-C. Chen, C. Song, Y. Nishino, Y. Kohmura, T. Ishikawa, D. Ramunno-Johnson, T.-K. Lee, and S.H. Risbud, *Phys. Rev. Lett.* 97, 215503 (2006).
43. C. Song, R. Bergstrom, D. Ramunno-Johnson, H. Jiang, D. Paterson, M.D. de Jonge, I. McNulty, J. Lee, K.L. Wang, and J. Miao, *Phys. Rev. Lett.* 100, 025504 (2008).
44. A. Barty, S. Marchesini, H.N. Chapman, C. Cui, M.R. Howells, D.A. Shapiro, A.M. Minor, J.C.H. Spence, U. Weierstall, J. Ilavsky, A. Noy, S.P. Hau-Riege, A.B. Artyukhin, T. Baumann, T. Willey, J. Stolken, T. van Buuren, and J.H. Kinney, *Phys. Rev. Lett.* 101, 055501 (2008).
45. R.L. Sandberg, A. Paul, D.A. Raymondson, S. Hädrich, D.M. Gaudiosi, J. Holtsnider, R.I. Tobey, O. Cohen, M.M. Murnane, H.C. Kapteyn, C. Song, J. Miao, Y. Liu, and F. Salmassi, *Phys. Rev. Lett.* 99, 098103 (2007).
46. R.L. Sandberg, C. Song, P.W. Wachulak, D.A. Raymondson, A. Paul, B. Amirbekian, E. Lee, A.E. Sakdinawat, C. La-O-Vorakiat, M.C. Marconi, C.S. Menoni, M.M. Murnane, J.J. Rocca, H.C. Kapteyn, and J. Miao, *Proc. Natl. Acad. Sci.* 105, 24 (2008).
47. J.J. Turner, X. Huang, O. Krupin, K.A. Seu, D. Parks, S. Kevan, E. Lima, K. Kisslinger, I. McNulty, R. Gambino, S. Mangin, S. Roy, and P. Fischer, *Phys. Rev. Lett.* 107, 033904 (2011).
48. A. Barty, C. Caleman, A. Aquila, N. Timneanu, L. Lomb, T.A. White, J. Andreasson, D. Arnlund, S. Bajt, T.R.M. Barends, M. Barthelmess, M.J. Bogan, C. Bostedt, J.D. Bozek, R. Coffee, N. Coppola, J. Davidsson, D.P. DePonte, R.B. Doak, T. Ekeberg, V. Elser, S.W. Epp, B. Erk, H. Fleckenstein, L. Foucar, P. Fromme, H. Graafsma, L. Gumprecht, J. Hajdu, C.Y. Hampton, R. Hartmann, A. Hartmann, G. Hauser, H. Hirsemann, P. Holl, M.S. Hunter, L. Johansson, S. Kassemeyer, N. Kimmel, R.A. Kirian, M. Liang, F.R.N.C. Maia, E. Malmerberg, S. Marchesini, A.V. Martin, K. Nass, R. Neutze, C. Reich, D. Rolles, B. Rudek, A. Rudenko, H. Scott, I. Schlichting, J. Schulz, M.M. Seibert, R.L. Shoeman, R.G. Sierra, H. Soltau, J.C.H. Spence, F. Stellato, S. Stern, L. Struder, J. Ullrich, X. Wang, G. Weidenspointner, U. Weierstall, C.B. Wunderer, and H.N. Chapman, *Nat. Photon.* 6, 35 (2012).

49. R. Neutze, R. Wouts, D. van der Spoel, E. Weckert, and J. Hajdu, *Nature* 406, 752 (2000).
50. M.J. Bogan, W.H. Benner, S. Boutet, U. Rohner, M. Frank, A. Barty, M.M. Seibert, F. Maia, S. Marchesini, S. Bajt, B. Woods, V. Riot, S.P. Hau-Riege, M. Svenda, E. Marklund, E. Spiller, J. Hajdu, and H.N. Chapman, *Nano Lett.* 8, 310 (2007).
51. R. Hegerl and W. Hoppe, *Berichte Bunsengesellschaft Phys. Chem.* 74, 1148 (1970).
52. H.M.L. Faulkner and J.M. Rodenburg, *Phys. Rev. Lett.* 93, 023903 (2004).
53. O. Bunk, M. Dierolf, S. Kynde, I. Johnson, O. Marti, and F. Pfeiffer, *Ultramicroscopy* 108, 481 (2008).
54. A.M. Maiden, M.J. Humphry, M.C. Sarahan, B. Kraus, and J.M. Rodenburg, *Ultramicroscopy* 120, 64 (2012).
55. M. Guizar-Sicairos, A. Diaz, A. Menzel, and O. Bunk, *Proc. SPIE* 8011, 80118F (2011).
56. A. Schropp, R. Hoppe, J. Patommel, D. Samberg, F. Seiboth, S. Stephan, G. Wellenreuther, G. Falkenberg, and C.G. Schroer, *Appl. Phys. Lett.* 100, 253112 (2012).
57. J.M. Rodenburg, A.C. Hurst, A.G. Cullis, B.R. Dobson, F. Pfeiffer, O. Bunk, C. David, K. Jefimovs, and I. Johnson, *Phys. Rev. Lett.* 98, 034801 (2007).
58. P. Thibault, M. Dierolf, A. Menzel, O. Bunk, C. David, and F. Pfeiffer, *Science* 321, 379 (2008).
59. P. Trtik, A. Diaz, M. Guizar-Sicairos, A. Menzel, and O. Bunk, *Cem. Concr. Compos.* 36, 71 (2013).
60. Y. Takahashi, A. Suzuki, N. Zettsu, Y. Kohmura, K. Yamauchi, and T. Ishikawa, *Appl. Phys. Lett.* 99, 131905 (2011).
61. A. Tripathi, J. Mohanty, S.H. Dietze, O.G. Shpyrko, E. Shipton, E.E. Fullerton, S.S. Kim, and I. McNulty, *Proc. Natl. Acad. Sci.* 108, 13393 (2011).
62. A. Schropp, P. Boye, A. Goldschmidt, S. Hönig, R. Hoppe, J. Patommel, C. Rakete, D. Samberg, S. Stephan, S. Schöder, M. Burghammer, and C.G. Schroer, *J. Microsc.* 241, 9 (2011).
63. G.J. Williams, H.M. Quiney, B.B. Dhal, C.Q. Tran, K.A. Nugent, A.G. Peele, D. Paterson, and M.D. de Jonge, *Phys. Rev. Lett.* 97, 025506 (2006).
64. K.A. Nugent, A.G. Peele, H.N. Chapman, and A.P. Mancuso, *Phys. Rev. Lett.* 91, 203902 (2003).
65. K.A. Nugent, A.G. Peele, and H.M. Quiney, *Proc. SPIE* 5917, 59170A (2005).
66. K.A. Nugent, A.G. Peele, H.M. Quiney, and H.N. Chapman, *Acta Crystallogr. A* 61, 373 (2005).
67. H.M. Quiney, K.A. Nugent, and A.G. Peele, *Opt. Lett.* 30, 1638 (2005).
68. R.H.T. Bates, *Comput. Vis. Graph. Image Process.* 25, 205 (1984).
69. T.A. Pitts and J.F. Greenleaf, *IEEE Trans. Ultrason. Ferroelectr. Freq. Control* 50, 1035 (2003).
70. H.M. Quiney, A.G. Peele, Z. Cai, D. Paterson, and K.A. Nugent, *Nat. Phys.* 2, 101 (2006).
71. C.M. Kewish, M. Guizar-Sicairos, C. Liu, J. Qian, B. Shi, C. Benson, A.M. Khounsary, J. Vila-Comamala, O. Bunk, J.R. Fienup, A.T. Macrander, and L. Assoufid, *Opt. Express* 18, 23420 (2010).
72. G.J. Williams, H.M. Quiney, A.G. Peele, and K.A. Nugent, *New J. Phys.* 12, 035020 (2010).
73. B. Abbey, K.A. Nugent, G.J. Williams, J.N. Clark, A.G. Peele, M.A. Pfeifer, M. De Jonge, and I. McNulty, *Nat. Phys.* 4, 394 (2008).
74. J.N. Clark, G.J. Williams, H.M. Quiney, L. Whitehead, M.D. de Jonge, E. Hanssen, M. Altissimo, K.A. Nugent, and A.G. Peele, *Opt. Express* 16, 3342 (2008).
75. B. Abbey, G.J. Williams, M.A. Pfeifer, J.N. Clark, and C.T. Putkunz, *Appl. Phys. Lett.* 93, 214101 (2008).
76. D. Vine, G. Williams, K. Nugent, B. Abbey, M. Pfeifer, J. Clark, A. Peele, M.D. Jonge, and I. McNulty, *Phys. Rev. A* 80, 063823 (2009).
77. C.T. Putkunz, J.N. Clark, D.J. Vine, G.J. Williams, M.A. Pfeifer, E. Balaur, I. McNulty, K.A. Nugent, and A.G. Peele, *Phys. Rev. Lett.* 106, 013903 (2011).
78. C.T. Putkunz, M.A. Pfeifer, A.G. Peele, G.J. Williams, H.M. Quiney, B. Abbey, K.A. Nugent, and I. McNulty, *Opt. Express* 18, 11746 (2010).
79. I. Peterson, B. Abbey, C.T. Putkunz, D.J. Vine, G.A. van Riessen, G.A. Cadenazzi, E. Balaur, R. Ryan, H.M. Quiney, I. McNulty, A.G. Peele, and K.A. Nugent, *Opt. Express* 20, 24678 (2012).
80. J.C.H. Spence, U. Weierstall, and M. Howells, *Ultramicroscopy* 101, 149 (2004).
81. I.K. Robinson, C.A. Kenney-Benson, and I.A. Vartanyants, *Phys. B: Condens. Matter* 336, 56 (2003).
82. I.A. Vartanyants and I.K. Robinson, *Opt. Commun.* 222, 29 (2003).
83. I.A. Vartanyants and I.K. Robinson, *J. Phys.: Condens. Matter* 13, 10593 (2011).
84. H.M. Quiney, *J. Mod. Opt.* 57, 1109 (2010).
85. S. Flewett, H.M. Quiney, C.Q. Tran, and K.A. Nugent, *Opt. Lett.* 34, 2198 (2009).
86. C.Q. Tran, G.J. Williams, A. Roberts, S. Flewett, A.G. Peele, D. Paterson, M.D. de Jonge, and K.A. Nugent, *Phys. Rev. Lett.* 98, 224801 (2007).
87. A. Starikov and E. Wolf, *J. Opt. Soc. Am.* 72, 923 (1982).
88. L.W. Whitehead, G.J. Williams, H.M. Quiney, D.J. Vine, R.A. Dilanian, S. Flewett, K.A. Nugent, A.G. Peele, E. Balaur, and I. McNulty, *Phys. Rev. Lett.* 103, 243902 (2009).
89. B. Chen, B. Abbey, R. Dilanian, E. Balaur, G. van Riessen, M. Junker, C.Q. Tran, M.W.M. Jones, A.G. Peele, and I. McNulty, *Phys. Rev. B* 86, 235401 (2012).
90. H.M. Quiney and K.A. Nugent, *Nat. Phys.* 7, 142 (2011).
91. R.A. Dilanian, V.A. Streltsov, H.M. Quiney, and K.A. Nugent, *Acta Crystallogr. A* 69(Pt 1), 108 (2013).
92. P. Thibault and A. Menzel, *Nature* 494, 68 (2013).
93. C. Spielmann, N.H. Burnett, S. Sartania, R. Koppitsch, M. Schnürer, C. Kan, M. Lenzner, P. Wobrauschek, and F. Krausz, *Science* 278, 661 (1997).
94. B. Chen, R.A. Dilanian, S. Teichmann, B. Abbey, A.G. Peele, G.J. Williams, P. Hannaford, L. Van Dao, H.M. Quiney, and K.A. Nugent, *Phys. Rev. A* 79, 23809 (2009).
95. B. Abbey, L.W. Whitehead, H.M. Quiney, D.J. Vine, G.A. Cadenazzi, C.A. Henderson, K.A. Nugent, E. Balaur, C.T. Putkunz, and A.G. Peele, *Nat. Photon.* 5, 420 (2011).
96. W. Berg, *Naturwissenschaften* 19, 391 (1931).
97. C.S. Barrett, *Trans. AIME* 161, 15 (1945).
98. A. Guinier and J. Tennevin, *Acta Crystallogr.* 2, 133 (1949).
99. A.R. Lang, *J. Appl. Phys.* 29, 597 (1958).
100. D.R. Black and G.G. Long (NIST Special Publication 960-10, 2004).
101. F. Hofmann, B. Abbey, X. Song, I. Dolbnya, and A.M. Korsunsky, *Int. J. Mod. Phys B* 24, 279 (2010).
102. S. Ravy, D.L. Bolloc'h, R. Currat, A. Fluerasu, C. Mocuta, and B. Dkhil, *Phys. Rev. Lett.* 98, 105501 (2007).
103. H. Bei, S. Shim, E.P. George, M.K. Miller, E.G. Herbert, and G.M. Pharr, *Scr. Mater.* 57, 397 (2007).
104. V.L.R. Jacques, S. Ravy, D. Le Bolloc'h, E. Pinsolle, M. Sauvage-Simkin, and F. Livet, *Phys. Rev. Lett.* 106, 065502 (2011).
105. P.F. Fewster, *Crit. Rev. Solid State Mater. Sci.* 22, 69 (1997).
106. I.K. Robinson, I.A. Vartanyants, G.J. Williams, M.A. Pfeifer, and J.A. Pitney, *Phys. Rev. Lett.* 87, 195505 (2001).
107. M.A. Pfeifer, G.J. Williams, I.A. Vartanyants, R. Harder, and I.K. Robinson, *Nature* 442, 63 (2006).
108. P. Godard, G. Carbone, M. Allain, F. Mastropietro, G. Chen, L. Capello, A. Diaz, T.H. Metzger, J. Stangl, and V. Chamard, *Nat. Commun.* 2, 568 (2011).
109. J.N. Clark, X. Huang, R. Harder, and I.K. Robinson, *Nat. Commun.* 3, 993 (2012).
110. M.C. Newton, S.J. Leake, R. Harder, and I.K. Robinson, *Nat. Mater.* 9, 120 (2010).
111. V. Favre-Nicolin, F. Mastropietro, J. Eymery, D. Camacho, Y.M. Niquet, B.M. Borg, M.E. Messing, L.E. Wernersson, R.E. Algra, E.P.A.M. Bakkers, T.H. Metzger, R. Harder, and I.K. Robinson, *New J. Phys.* 12, 035013 (2010).

112. S.O. Hruszkewycz, M.V. Holt, C.E. Murray, J. Bruley, J. Holt, A. Tripathi, O.G. Shpyrko, I. McNulty, M.J. Highland, and P.H. Fuoss, *Nano Lett.* 12, 5148 (2012).
113. Y. Takahashi, A. Suzuki, S. Furutaku, K. Yamauchi, Y. Kohmura, and T. Ishikawa, *Phys. Rev. B* 87, 121201 (2013).
114. J.N. Clark, L. Beitra, G. Xiong, A. Higginbotham, D.M. Fritz, H.T. Lemke, D. Zhu, M. Chollet, G.J. Williams, M. Messerschmidt, B. Abbey, R.J. Harder, A.M. Korsunsky, J.S. Wark, and I.K. Robinson, *Science* 341, 56 (2013).
115. S.P. Hau-Riege, A. Graf, T. Döppner, R.A. London, J. Krzywinski, C. Fortmann, S.H. Glenzer, M. Frank, K. Sokolowski-Tinten, M. Messerschmidt, C. Bostedt, S. Schorb, J.A. Bradley, A. Lutman, D. Rolles, A. Rudenko, and B. Rudek, *Phys. Rev. Lett.* 108, 217402 (2012).